

## JP2.7 IMPACTS OF BEAM BROADENING AND EARTH CURVATURE ON 3D VARIATIONAL RADAR DATA ASSIMILATION WITH TWO DOPPLER RADARS

Guoqing Ge<sup>1,2</sup>, Jidong Gao<sup>1</sup>, Keith Brewster<sup>1</sup>, and Ming Xue<sup>1,2</sup>

<sup>1</sup>*Center for Analysis and Prediction of Storms and* <sup>2</sup>*School of Meteorology,*  
*University of Oklahoma, Norman, OK 73072*

### 1. INTRODUCTION

The operational WSR-88D Doppler radar network (NEXRAD) is an important tool for real-time detection and warning of hazardous weather (Crum and Alberty, 1993; Crum et al., 1998; Serafin and Wilson, 2000). It is also an essential observing system for initializing non-hydrostatic, storm-resolving (i.e., horizontal grid spacing on the order of 1 km) numerical weather prediction (NWP) models (e.g., Lilly, 1990; Droegemeier, 1990, 1997). To assimilate these radar data into NWP models, it is necessary to accurately determine the spatial locations of individual radar measurements. Because the propagation path of the electromagnetic waves can be affected by the refractivity of the atmosphere, the propagation path or the ray path is usually not a straight line. A suitable ray path equation is therefore needed. The local direction of the ray path also affects the radial velocity forward operator that projects the Cartesian velocity components on the model grid to the local radial direction in data assimilation systems.

Most early radar data assimilation studies used relatively simple ray path equations in the forward operator formulation which are based on the Cartesian geometry, essentially assuming a flat earth (e.g., Sun 1991, 1997, 1998; Gao et al., 1998, 2004; Weygandt et al., 2002a,b; Shapiro et al., 2003). Brewster (2003) applied complete ray path equations into Advanced Regional Prediction systems's Data Assimilation System (ADAS). But his study did not cover the impact of these ray path equations on the ADAS radar data assimilation system. Gao et al. (2006, hereafter Gao06) has shown that using

simplified radar ray path equations introduces errors that are significant for ranges beyond 30 km. In that paper, a set of four-thirds earth-radius ray path equations is recommended, especially at low elevation angles. However, Gao06 mainly addresses the error in physical location of individual radar measurement. It is also of interest to study how, and to what extent, the neglecting of earth curvature and radar beam broadening will affect the results of storm-scale radar data.

In order to compute most accurately the model counterpart of radial wind, one must integrate over all possible model grid points within the radar beam main lobe, which broadens with range. Most radar data assimilation studies don't consider this beam broadening effect. Recently, Wood and Brown (1997) introduced a power gain weighted average in the radar forward observation operator in their study on the effects of radar sampling on velocity signatures of mesocyclones and tornadoes. Sun and Crook (2001) incorporated a similar beam broadening equation in their 4DVAR radar analysis system. Salonen (2002) approximated the beam broadening effect with a Gaussian function (Probert-Jones, 1962) in the vertical direction and demonstrate slightly positive impact on radar analysis using HIRLAM 3DVAR system. Xue et al (2006), Tong (2006) used a power-gain-based sampling in vertical direction to compute the model counterpart of radial velocity in their EnKF works.. All these treatment are more reasonable since it is more close to the nature of the radar measurement. Caumont and Durocq (2008) showed that neglecting the beam broadening can cause large

errors at farther gates in the simulation of radar data. However, a detailed study of the effect of beam broadening in storm-scale data analysis and assimilation has not yet been investigated.

In this study, the effect of earth curvature and beam broadening in radar data assimilation is investigated using an idealized supercell tornadic thunderstorm. The ARPS 3DVAR system, described in Gao et al (2002; 2004) and Hu et al (2006b) is used for this purpose. The ARPS 3DVAR system is capable of analyzing radar radial velocity data along with conventional observations. It is usually used together with the cloud analysis system to initialize hydrometer related variables and provide a latent heating adjustment. For simplicity in studying the radial velocity effects, in this paper only the simulated radial winds derived from an idealized thunderstorm are used and the cloud analysis is not used. In the ARPS 3DVAR system, the mass continuity weak constraint is included in the cost function that serves to link three wind components together and helps to improve wind analysis.

This paper is organized as the following. In sections 2 and 3, we will briefly introduce the radar forward observation operator and the ARPS 3DVAR system respectively. In section 4, the model configuration and experiment design are discussed. The results are presented in section 5, and summary and discussion in section 6.

## 2. THE RADAR FORWARD OBSERVATION OPERATOR

Under the assumption that temperature and humidity are horizontally homogeneous so that the refractivity is a function only of height above ground, Doviak and Zrnice (1993) present a formulation that expresses the ray path in terms of a path following a curve of a sphere of radius,

$$a_e = \frac{a}{1 + a \left( \frac{dn}{dh} \right)} = k_e a \quad (1)$$

where  $a$  is the earth's radius and  $k_e$  is a multiplier which is dependent on the vertical gradient of refractive index of air,  $\frac{dn}{dh}$ . The refractive index of air,  $n$ , is a function of its temperature, pressure and humidity and is usually taken, subject to certain assumptions, as (Beam and Dutton 1968),

$$N = (n-1) \times 10^6 = 77.6P/T + 3.73 \times 10^{-5} e T^{-2} \quad (2)$$

where  $P$  is air pressure in hPa (including water vapor pressure),  $e$  is water vapor pressure in hPa, and  $T$  is air temperature in degrees K. It is convenient to use the quantity  $N$  called radio refractivity instead of  $n$ .  $N$  represents the departure of  $n$  from unity in parts per million.  $N$  has a value of about 300 (at the surface) and its variations can be considered more conveniently. In the above equation, the first term on the right hand side is known as the dry term, the second term is the moist term. The value of  $N$  can be computed from measurement of  $P$ ,  $T$ ,  $e$ . When the Standard Atmosphere is considered, it is found that  $k_e$  is equal to 4/3 (Doviak and Zrnice' 1993). This is often referred to as the "four-thirds earth radius model".

The following two equations relate  $h$  and the surface range (distance along the earth's surface),  $s$ , to radar-measurable parameters, the slant path,  $r$  and radar elevation angle,  $\theta_e$  (Doviak and Zrnice 1993),

$$s = k_e a \sin^{-1} \left( \frac{r \cos \theta_e}{k_e a + h} \right) \quad (3)$$

$$h = \left[ r^2 + (k_e a)^2 + 2rk_e a \sin \theta_e \right]^{1/2} - k_e a \quad (4)$$

To consider the curvature of the Earth, the radar forward observation operator can be written as the following equation:

$$v_r^* = u \cos \theta_e' \sin \phi + v \cos \theta_e' \cos \phi + (w - w_t) \sin \theta_e' \quad (5)$$

where  $\phi$  is radar azimuth angle,  $w_r$  is the terminal velocity of precipitation, and  $\theta_e'$  includes the effect of the curvature of the earth as the following:

$$\theta_e' = \theta_e + \tan^{-1} \left[ \frac{r \cos \theta_e}{k_e a + r \sin \theta_e} \right] \quad (6)$$

In this study, only effect of beam broadening in the vertical direction is considered. The reason is as the following. In storm-scale NWP, the horizontal resolution is normally 1km~3km and a 1° half-power beam width will measure about 3490 m at a surface range of 200 km. So a beam lobe at a surface range of 200 km and gate spacing less than 1-km will enclose only 1~3 horizontal grid points, even at 1-km grid spacing, which we judge to be too few to have a material difference. However, the vertical resolution of NWP models typically ranges from 20 to 500 m and a beam lobe at a range of 200 km can span more than seven vertical grid points, much greater than the two grid points used to compute the model counterpart of radial wind with linear interpolation. On the other hand, the height of the lowest ray above the ground will increase rapidly with range (Gao et al., 2006). At a surface range of 100 km, the height of at 0.5 degree ray above the ground is about 1.7 km and at 200 km it is about 4 km. So there may be little information observed of the boundary layer, especially far from the radar. Considering beam broadening in the radar forward observation operator may also spread information below the center of the lowest ray, affecting the assimilation results.

Following Rihan et al. (2008), the observation operator for mapping data from multiple vertical model levels onto elevation angles is formulated as:

$$V_{r,e} = H_e(V_r) = \left( \sum G V_r \Delta z \right) / \left( \sum G \Delta z \right) \quad (7)$$

where  $V_{r,e}$  is the radial velocity on an elevation angle,  $H_e$  is the radar forward observation operator,  $V_r$  is the model counterpart of radial velocity,  $\Delta z$  is

the vertical model grid spacing.  $G$  describes the power gain distribution within the radar beam and is formulated as  $G = e^{-\alpha^2 / (2\beta^2)}$  with  $\alpha$  as the distance from the center of the radar beam in radians and  $\beta$  as the half-power beamwidth in radians. The summation is over vertical model grid points enclosed by the half-power beam lobe.

### 3. THE ARPS 3DVAR SYSTEM

Following Gao et al. (2004), the standard cost function of 3DVAR can be written as,

$$J(\mathbf{x}) = \frac{1}{2} (\mathbf{x} - \mathbf{x}^b)^T \mathbf{B}^{-1} (\mathbf{x} - \mathbf{x}^b) + \frac{1}{2} [H(\mathbf{x}) - \mathbf{y}^o]^T \mathbf{R}^{-1} [H(\mathbf{x}) - \mathbf{y}^o] + J_c(\mathbf{x}) \quad (8)$$

where the first term on the right hand side measures the departure of the analysis vector,  $\mathbf{x}$ , from the background,  $\mathbf{x}^b$ , weighted by the inverse of the background error covariance matrix  $\mathbf{B}$ . In the current ARPS 3DVAR system, the analysis vector  $\mathbf{x}$  contains the three wind components ( $u$ ,  $v$ , and  $w$ ), potential temperature ( $\theta$ ), pressure ( $p$ ) and water vapor mixing ratio ( $q_v$ ). The second, observation term, measures the departure of the analysis from the observation vector,  $\mathbf{y}^o$ . In this study,  $\mathbf{y}^o$  only includes radar radial velocity data. The analysis is projected to the observation space by the forward operator  $H$  which is defined by equations (1) ~ (7) and interpolation operator from model grid points to radar observation locations. The observation term is weighted by the inverse of observation error covariance matrix  $\mathbf{R}$  that includes the both instrument and representativeness errors. Because only radial velocity data are used in the analysis system, only wind components will be updated during the minimization process.

Term  $J_c(\mathbf{x})$  in Eq. (8) represents dynamic or equation constraints. By defining  $\sqrt{\mathbf{B}}\mathbf{v} = (\mathbf{x} - \mathbf{x}^b)$ , the cost function is changed into incremental form:

$$J_{inc}(\mathbf{v}) = \frac{1}{2}\mathbf{v}^T\mathbf{v} + \frac{1}{2}(\mathbf{HB}^{1/2}\mathbf{v} - \mathbf{d})^T \mathbf{R}^{-1}(\mathbf{HB}^{1/2}\mathbf{v} - \mathbf{d}) + J_c(\mathbf{v}) \quad (9)$$

where  $\mathbf{H}$  is the linearized version of  $H$  and  $\mathbf{d} \equiv \mathbf{y}^o - H(\mathbf{x}^b)$ . In the current version of ARPS 3DVAR system, the cross-correlations between variables are not included in the background error covariances. The spatial covariances for background error are modeled by a recursive filter (Purser, 2003a, 2003b). The corresponding covariance matrix,  $\mathbf{R}$ , is diagonal, and its diagonal elements are specified according to the estimated observation errors.

In the ARPS 3DVAR, the mass continuity equation is imposed as a weak constraint. This constraint builds up the relationship among the three wind components. Gao et al (1999; 2004) found that this constraint is very effective in producing suitable analyses of vertical velocity. When a stretched grid strategy is used in the vertical direction, a special treatment (Hu et al. 2006a, 2006b), which assigns different weighting coefficients in horizontal and vertical direction, is needed to apply this constraint. More recently, the modified ARPS model equations are included as weak constraints in the 3DVAR scheme. These newly introduced constraints couple the wind components with thermodynamic variables (Ge et al. 2007). In this study, for simplicity, only the mass continuity constraint is included because our focus is to disclose the impact of beam broadening and earth curvature on storm-scale data assimilation.

#### 4. EXPERIMENTAL DESIGN

In this study, we evaluate the impact of beam broadening and earth curvature on data assimilation system using simulated data. Such simulation

experiments are usually referred to as observing system simulation experiments (OSSEs). The ARPS model is used in a 3D cloud model mode. The 20 May 1977 Del City, Oklahoma tornadic supercell storm is used to conduct several series of experiments. This storm has been thoroughly studied by multiple Doppler analysis and numerical simulation (Ray et al. 1981; Klemp et al. 1981; and Klemp and Rotunno 1983).

The model is configured as the following:  $67 \times 67 \times 35$  grid points and  $1\text{km} \times 1\text{km} \times 0.5\text{km}$  grid intervals for the x, y, and z directions, respectively, so as to establish a physical domain of  $64 \times 64 \times 16$  km. The simulation starts with a modified sounding (as in Klemp et al, 1981) which favors the development of a supercell thunderstorm. The thermal bubble has a 4 K perturbation, and is centered at  $x=48$  km,  $y=16$  km and  $z=1.5$  km with the lower-left corner of the domain as the origin. The radius of the bubble is 10 km in the x and y directions and 1.5 km in the z direction. The three-category ice microphysical scheme of Lin et al. (1983) is used together with a 1.5-order turbulent kinetic energy subgrid parameterization. Open boundary conditions are used for the lateral boundaries and rigid wall conditions for the top and bottom boundaries. An upper-level Rayleigh damping layer is also included to inhibit wave reflection from the top of the model.

The simulation runs for 3 hr. The initial convective cell strengthens over the first 20 min and begins to split into two cells around 1 hr. To keep the right-moving storm near the center of the model domain, a mean storm speed ( $U=3 \text{ ms}^{-1}$ ,  $V=14 \text{ ms}^{-1}$ ) is subtracted from the sounding. At about 2 hr into the simulation, the right mover is still near the center of the domain as expected and the left mover is located at the northwest corner. Fig.1a and Fig. 2a shows horizontal and vertical cross sections of simulated wind, vertical velocity at 2 hr respectively (vertical cross section is plotted through line A-B in Fig. 1a). A strong rotating updraft (with maximum vertical velocity exceeding  $29 \text{ ms}^{-1}$ ) and associated low-level

downdraft are evident near the center of the domain. The updraft tilts eastward in the upper part of the troposphere. The evolution of the simulated storm is qualitatively similar to that described by Klemp and Wilhelmson (1981). After 2 h, the major storm gradually moves a little bit to the southeastern corner of the model domain, and remains a very strong supercell structure until the end of simulation at 3 h (Fig 7a-c).

Three series of pseudo radar radial observations from two Doppler radars are obtained by sampling the evolution of this simulated storm every 5 min from 2 hr min to 3 hr using radar forward operators expressed in eq. (1)-(7). The first series of simulated data are obtained from the simulated wind field fixed at  $t=2$  h, but as a function of varied radar locations. The first radar's  $x$  coordinate is set at  $x=33$  km relative to the origin of model domain (at lower left corner at this time), while its  $y$  coordinate is varied in increments of 10 km from  $y=-190$  km to  $y=10$  km. A second radar is set at position  $y=25$  km while its  $x$  coordinate is varied from  $x=0$  km to  $x=-200$  km in intervals of 10 km. In this way, we are able to test the impact of the beam broadening and the earth curvature as a function of distance from the center of the storm ranging from about 20 km to 220 km. The center of the storm is roughly estimated to be (32.5 km, 22.5 km). The second series of radial velocity observations are obtained every 5 minutes from model simulation between 2 and 3 h using the same forward operator, but two radars are at fixed locations (33 km, 40 km) and (30 km, 25 km) respectively. In this case, the surface range between the storm center and either of the radars is about 60 km. The third series of pseudo observations are sampled in a similar way to the second one, but two radars at fixed locations (33 km, 130 km) and (120 km, 25 km). In this case the distance between the storm center and either of the radars is about 150 km.

The elapsed times for the radars to obtain the volume scans are neglected, and thus we assume that the radial wind observations are simultaneous.

For simplicity, the two radars will cover the entire horizontal physical grids (i.e.  $64 \times 64$  km) which assumes that the radars sweep almost continuously in horizontal direction. The elevation angle spacing is assumed to be  $1^\circ$  with the first elevation angle is  $0.5^\circ$ . The simulated data are only specified in precipitation regions (where reflectivity is greater than zero). In order to simulate the radar measurement statistical error,  $1 \text{ ms}^{-1}$  random error is added to the radial velocities in the pseudo observation data.

Corresponding to the first series of radial wind observations, three categories of 21 data analysis experiments (see Table 1, which lists all experiments) will be conducted at  $t=2$  h with varied surface ranges between radar location and storm center. In the first category of experiments, both the effect of beam broadening and the effects of earth curvature are considered using the radar forward observation operator as defined in Eqs. 1-7. They will be referred as CNTL1 experiments (label 1 means at single time level). In the second category of experiments, the effect of beam broadening is not considered and Eq. (7) will be replaced with a simple tri-linear interpolation scheme. It will be referred as NoBB1 experiments. In the third category of experiments, the effect of earth curvature will not be considered and Eq. (3) ~ (6) will be replaced with the commonly used Cartesian radar forward operator (Gao et al. 1999). It will be referred as NoCV1 experiments. The distance between the storm and the radar vary from 20 km to 220 km at an interval of 10 km for both radars. So each individual experiment will be referred by its category name followed by the distance in km, as described above, e.g. CNTL1\_60, NoBB1\_60, NoCV1\_60, etc.

Corresponding to the second series of pseudo observations, three intermittent data assimilation experiments (see Table 1) are performed with an interval of 5 minutes and a window covering  $t=2$  h to  $t=3$  h of the model simulation. For these three experiments, the distance from the radar to the storm

center is about 60 km when the data assimilation experiments begin. These three experiments are referred as CNTLM\_60, NoBBM\_60, NoCVM\_60 experiments with similar literal meaning as the above (where the label M is added to denote multiple time levels). Corresponding to the third series of pseudo observations, three more intermittent data assimilation experiments (see Table 1) are performed. The setting is same as above, but the distance between radar location and storm center is changed to 150 km at the beginning of data assimilation. Similarly, these three more experiments are named CNTLM\_150, NoBBM\_150, NoCVM\_150. These six experiments are designed to assess the impact of the beam broadening and the earth curvature on radar data assimilation over a data assimilation window while radar sites are near, or far away from a storm. There are 12 assimilation cycles with 5 minute interval in these 6 experiments. The ARPS 3DVAR system is used to obtain the model initial condition first, and then the ARPS system runs for a five minute forecast starting from this initial analysis. This intermittent assimilation cycle is applied every five minutes until the end of assimilation period.

To compare the accuracy of the analysis from different experiments, the RMS error statistics of the horizontal winds ( $V_h$ ) and scalar model variables ( $s$ ) between the experiments and the simulation run are computed using the following equations:

$$RMS\_Vh = \sqrt{\frac{\sum_{i=1}^N (u - u_{simu})_i^2 + \sum_{i=1}^N (v - v_{simu})_i^2}{2N}}$$

$$RMS\_s = \sqrt{\frac{\sum_{i=1}^N (s - s_{simu})_i^2}{N}}$$

where  $N$  is the total number of 3-dimensional grid points within physical domain, the subscript *simu* stands for the data from the simulation run. The

computation of the RMS error statistics is only done over model grid points where the reflectivity (estimated from the local hydrometeor mixing ratios) of the simulation run is greater than 5 dBZ.

## 5. RESULTS OF EXPERIMENTS

### 5.1 The impact on 3DVAR wind analysis at t=2 hr time level

As stated above, the purpose of first series of experiments is to test the impact of beam broadening and earth curvature on 3DVAR wind analysis at a single time level. For ease in comparison of the results of experiments, the variations of RMS errors for NoBB1 and NoCV1 are plotted separately in Fig. 1 and Fig. 2 along with that for CNTL1. The horizontal section at z=3.5km AGL and the vertical cross section at y=22.5km of wind fields for the truth simulation and all the three experiments are plotted in Fig 3-6.

We first discuss the impact of beam broadening. The RMS error of the horizontal winds and the vertical velocities plotted as a function of the distance for both CNTL1 and NoBB1 experiments are shown in Fig. 1. It is found that the RMS error differences for both horizontal winds and vertical velocities between these 21 CNTL1 experiments and their corresponding NoBB1 experiments gradually increase as the distance between the storm center and radar locations increase. These differences are less than  $0.5 \text{ ms}^{-1}$  for horizontal winds, representing half the applied statistical error, and less than  $0.2 \text{ ms}^{-1}$  for vertical velocities within the range of 60 km. Beyond 60 km, the differences for horizontal winds becomes more noticeable, reaching over  $1 \text{ ms}^{-1}$  at the range of 220 km, while the difference for vertical velocity shows little change. This means that additional error due to the neglect of beam broadening are gradually introduced in NoBB1 experiments but the maximum error is no more than the statistical error in the observations.

The variation in the RMS errors for horizontal winds and vertical velocities as a function of distance

for experiment NoCV1 is plotted in Fig. 2, and that for CNTL1 are also re-plotted here for ease in comparison. It is easily identified that the neglecting of the earth curvature can lead to very large RMS errors in the analysis of horizontal winds especially beyond 60 km. It exhibits an extra  $7.2 \text{ ms}^{-1}$  RMS error of horizontal winds compared to CNTL1 experiment at the range of 220 km (Fig. 2a). The RMS error differences for vertical velocities between CNTL1 and NoCV1 experiments are evident when the surface range is over 150 km (Fig. 2b). So in the sense of the evolution of RMS errors, we can conclude that overlooking the earth curvature has a much greater negative impact on variational wind analysis than the neglect of beam broadening.

As the RMS statistics suggest, the differences in the 3-D wind fields among all three categories of experiments CNTL1, NoBB1 and NoCV1 experiments should be very small when the distance between the storm and radars is less than 60 km. Fig. 3 and Fig. 4 confirm this conclusion. Fig. 3 shows that the horizontal wind and vertical velocity fields at 3.5 km AGL for the truth simulation, CNTL1\_60, NOBB1\_60, and NOCA1\_60 for the case where the radar is 60 km from the storm. Though the 3DVAR analysis is not perfect, the horizontal cyclonic rotation associated with the right and left movers are clearly evident in all three experiments (Fig. 3b, c, d). They are all pretty close to the truth simulation (Fig. 3a). The analyzed maximum vertical velocities (Fig. 4b, c, d) for all three categories of experiments are generally several meters per second weaker than the truth simulation, but the pattern is nearly the same for all three experiments. So the error from neglecting both beam broadening and earth curvature at this range is pretty small.

When the distance between the storm and radar location is greater than 150 km, the differences among these experiments become larger and can no longer be ignored. As an example, horizontal cross sections at  $z=3.5 \text{ km}$  and vertical cross sections are plotted as in Fig. 5 and Fig. 6 for the surface range of

150 km. It is clearly evident that the rotation signature near the center of the storm in Fig 5a for CNTL1\_150 is stronger than that in Fig. 5b for NoBB1\_150. Also Fig. 6a shows a much stronger and deeper rotation updraft than Fig 6b. The maximum vertical velocity in Fig. 6a is  $22.76 \text{ m/s}$ , much closer to simulation result (as shown in Fig 4a) than that in Fig. 6b which is only  $14.36 \text{ m/s}$ . Apparently, CNTL1\_150 experiment does a better job for the wind analysis than NoBB1\_150 in which no effect of beam broadening is considered.

For experiment NoCV1\_150 in which the influence of the earth's curvature is not considered, Fig 5c shows that the perturbation horizontal winds are unexpectedly strong and quite noisy. The signatures of cyclonic rotation within each of the cells are not so well analyzed. Although the strength of the major updraft in Fig 6c is well captured, just as in Fig 6a of CNTL1\_150, the updraft in Fig 6c is incorrectly positioned in the vertical, about 1 km below than that in Fig 6a. All these distorted features are evidently caused by the neglect of the effect of the earth curvature in the radar forward observation operator.

It should be noted that the wind analysis generally becomes worse even in CNTL1\_150km experiment since in the current situation the radars are 150 km from the radar.

It is demonstrated that the impacts of both the beam broadening and earth curvature are dependent on the surface range between the center of the storm and the radar location. It appears that within a range of 60 km, both the impacts of beam broadening and earth curvature can be neglected. As the distance increases beyond 60 km, more and more additional errors are introduced into the wind analysis from both earth curvature and beam broadening effects. Specifically, the neglect of the earth curvature exhibits much more negative impact than the neglect of the beam broadening. When the distance to the storm exceeds 150 km, overlooking the earth curvature and the beam broadening will both bring much more obvious negative impact on the 3-dimensional wind analysis. So the Cartesian ray path equation and a

simple interpolation are not recommended when the distance to the storm is greater than 150 km..

## 5.2 The impact on radar data assimilation cycles

To investigate how the errors introduced by neglecting of the beam broadening and the earth curvature are accumulated during an intermittent data assimilation and investigate how the retrievals of other model variables, such as potential temperature, moisture are impacted, two time series of data assimilation with 5 minutes interval are performed during a one-hour-long data assimilation period. As discussed in section 4, first three intermittent data assimilation experiments referred as CNTLM\_60, NoBBM\_60, NoCVM\_60 are conducted using data sampled from  $t=120$  min to  $t=180$  min of model simulation with the surface range between radar location and storm center is about 60 km when the data assimilation experiments begin. Three more experiments CNTLM\_150, NoBBM\_150, NoCVM\_150 are conducted for the surface range between the storm center and radar locations is 150 km at the beginning of data assimilation. The results from these six experiments are discussed in the following.

Fig. 7 shows the horizontal winds, perturbation potential temperature and reflectivity at 250 m AGL (first model level above surface) and Fig. 8 shows the horizontal wind and vertical velocity fields at 3.5 km AGL, at 140, 155 and 170 min of model time. Recall that the model assimilation begins at  $t=120$  min. They are shown for the truth simulation, cycled 3DVAR assimilation for experiments CNTLM\_60, NoBBM\_60 and No\_CVM\_60, as described in above. For all three experiments, Fig. 7d, j, g show that after 4 cycles at  $t = 140$  min, the assimilation has retrieved some weak potential temperature perturbations. Though no reflectivity is assimilated, the model established the reflectivity pattern quite similar to the truth simulation, although covering a smaller area after 20 minutes of assimilation. A small positive temperature

perturbation is found where there should be cooling (Fig. 7d, g, j). At the 3.5 km level (Fig. 8d, g, j), an updraft is established well at the correct location, and its strength and structure are quite similar to the truth (Fig. 8a). After three more analysis cycles at  $t = 155$  min, the low-level flow immediately underneath the storm cells becomes closer to the truth (Fig. 7e, h, k vs 7b) but the area of outflow and cold pool on the southwest side remain smaller than the truth. At the 3.5 km level, the perturbation horizontal winds and the updrafts are well captured in all three experiments by  $t= 155$  min (Fig. 8e, h, k vs 8b).

By  $t = 170$  min, the analysis is further improved. In fact, by this time, there are not significant differences from the truth in either the low-level and mid-level fields (Fig. 7f, i, m and Fig. 8f, l, m). Even a small downdraft beside the main updraft core is retrieved at this level for two experiments CNTLM\_60, and NoBBM\_60. General storm structures including the precipitation pattern are well retrieved during this 1 hr data assimilation in all three experiments though the results from NoCVM\_60 are not quite as good. This reinforces that the impacts of beam broadening and earth curvature on radar data assimilation cycles for retrieving other model variables which are not observed by two radars are generally small when the storm is not far from two radars.

Although the RMS error is generally not well suited as a verification metric for storm-scale phenomena, we use it here for comparison among different experiments while also visually comparing plotted fields to verify the result. The RMS errors for several analyzed fields are shown in Fig. 9. The RMS errors for  $V_h$  decrease with time, but very slowly. The variation of RMS errors for  $w$  are not stable, possibly because of small phase or position errors. The RMS errors for  $\theta'$  decrease for the first 40 minutes of assimilation, then increase with time again. Only the errors for  $q_v$  decrease nearly monotonically with time. The  $q_v$  RMS error is reduced to  $0.30 \text{ g kg}^{-1}$  in CNTLM\_60, and to  $0.33, 0.36 \text{ g kg}^{-1}$  in NoBBM\_60 and NoCVM\_60 respectively. Figure 9 generally

shows that the rms errors of  $V_h$ ,  $w$ ,  $\theta$ , and  $q_v$  stay very close for all three experiments though NoCVM\_60 has slightly larger errors in  $V_h$ . The RMS errors again suggest that the effect of beam broadening and earth curvature is generally small when the storm is not far from radar.

We now turn to the results for experiments CNTLM\_150, NoBBM\_150 and NoCVM\_150. Fig. 10 and Fig. 11 show that, in general, the results are significantly worse in all three experiments than the prior 60 km experiments. The overall storm structures are poorly resolved compared to CNTLM\_60, NoBBM\_60 and NoCVM\_60. But among the three experiments for the range of 150 km, the overall structure of the storm for CNTLM\_150 is the best and quite similar to those of the truth toward the end of the assimilation. At this time level, the analyzed mid-level flow, updraft, the surface cold pool, and precipitation pattern match the truth quite well (Fig. 10c and Fig. 11c vs Fig. 7c and Fig. 8c).

In experiment NoBBM\_150, the precipitation area is pretty small and the cold pool is very weak at 140 min, i.e. after 20 min of assimilation (Fig. 10d), but the pattern of horizontal winds and strength of updraft at the 3.5 km level is similar to the truth (Fig. 11d vs Fig. 8a). At 155 min, the analysis looks better, but both the horizontal wind and vertical velocity field look noisy, and there exist several small centers for positive, or negative contours which are not supported by the truth simulation (Fig. 11e vs Fig. 8b). At the end of the assimilation (Fig. 10f and Fig. 11f), the reflectivity and updraft pattern looks much closer to the truth. Clearly, at this very large radar range, the neglect of beam broadening worsen the assimilation results although the impact is limited and the internal structures of thunderstorms can be obtained by the end of 1 hr assimilation.

When the effect of earth curvature is not considered at the range of 150 km, the analyzed low-level cold pool, gust front, and precipitation pattern at  $t=170\text{min}$  differ markedly from those of the truth (Fig. 10g-i vs. Fig. 7a-c) and from the control assimilation

at this range (vs. Fig. 8a-c). At 155 min, the mid-level updraft appears broader and the pattern of horizontal flow is significantly different from the truth. The reflectivity core becomes distorted and the hook echo is poorly defined after 50 min assimilation (Fig. 10i vs Fig. 7c). Also at this time, there are a few spurious updrafts within the analysis domain (Fig. 11i). Overall, the analysis is significantly worsen when the effect of earth curvature is not considered at a range of 150 km.

The variations of the RMS error in horizontal wind ( $V_h$ ), vertical velocity ( $w$ ), perturbation potential temperature ( $\theta$ ) and perturbation water vapor mixing ratio ( $q_v$ ) are plotted in Fig. 12. It is demonstrated that the RMS errors in NoBBM\_150 are generally larger than that in CNTLM\_150 but do not deviate much from that standard. The NoCVM\_150 experiment yields the worst results with the largest rms errors during the 1 hr long assimilation period among all three experiments, especially for variables  $V_h$  and  $q_v$ . These error statistics also indicate that when a storm is 150 km from the radar, neglecting beam broadening and earth curvature produce significantly worse results for retrieved model variables than when the storm remains within 60 km during the data assimilation cycles.

## 6. SUMMARY AND CONCLUSION

To utilize high resolution radar radial velocity data in storm-scale data assimilation, it is necessary to compute the model counterpart of radial winds by converting  $u$ ,  $v$ ,  $w$  winds on model grids into radial velocity in radar coordinates. This is called the radar forward observation operator. The most accurate forward observation operator include considering the effect of beam broadening and the earth curvature. However, this may lead to higher computational cost that could impact the lead time of a forecast system or require additional computational resources. So a lot of research in recent years used a very simple form of radar observation operator by neglecting the two

effects mentioned above. In this study, we studied the effects of these assumptions on assimilating data from an idealized simulated supercell storm. It is shown that both the effects of beam broadening and earth curvature can only be neglected when the radar is near the storm, within 60 km, as demonstrated by this study.

For wind analysis at a single time, as the surface range increases, more and more additional error will be introduced into the analysis by the neglect of the two effects. The effect of beam broadening becomes evident and can cause relative large errors for ranges beyond 150 km. The effect of earth curvature is very significant when the surface range is beyond 60 km and it results in the storm features being placed in the wrong vertical location.

In two one-hour-long data assimilation experiments it is shown that the impact of both effects is not significant for retrieving unobserved model variables when the radars are relatively close to the storm (generally within 60 km). However, when the radars are far from the storm (especially beyond 150 km), not accounting for beam broadening has a rather small effect on the accuracy of assimilation results after one hour assimilation, while ignoring the earth's curvature leads to significant errors for retrieved model variables and reflectivity due to the vertical errors in data placement. The results of this study may provide useful guidance for application of radar radial velocity data to storm scale diagnostic studies as well as numerical weather prediction.

**Acknowledgments.** This research was supported by NSF grants ATM-0738370 and EEC-031347, ATM-0608168. Computations were performed at the Pittsburgh Supercomputing Center (PSC) and Oklahoma Supercomputing Center for Research and Education (OSKER).

## REFERENCES

- Bean B. R. and E. J. Dutton, 1968: *Radio Meteorology*, Dover Publication, 435 pp.
- Brewster, K. A., 2003: Phase-correcting data assimilation and application to storm scale numerical weather prediction. Part II: Application to a severe storm outbreak. *Mon. Wea. Rev.*, 131, 493-507.
- Caumont, O. and V. Ducrocq, 2008: What Should Be Considered When Simulating Doppler Velocities Measured by Ground-Based Weather Radars? *J. Appl. Meteor. Clim.*, 47, 2256–2262
- Crook, N. A., and J. Sun, 2002: Assimilating radar, surface, and profiler data for the Sydney 2000 Forecast Demonstration Project. *J. Atmos. Oceanic Technol.*, 19, 888-898.
- Crum, T. D., and R. L. Albert, 1993: The WSR-88D and the WSR-88D operational support facility. *Bull. Amer. Meteor. Soc.*, 74, 1669-1687.
- Crum, T. D., R. E. Saffle, and J. W. Wilson, 1998: An Update on the NEXRAD Program and Future WSR-88D Support to Operations. *Wea. and Forecasting*, 13, 253–262.
- Doviak, R. J., and D. S. Zmic, 1993: *Doppler Radar and Weather Observations*. Academic Press, 2nd Ed., 562pp.
- Droegemeier, K. K., 1990: Toward a science of storm-scale prediction. *Preprint, 16th Conf. on Severe Local Storms*, Kananaskis Park, Alberta, Canada, Amer. Meteor. Soc., 256-262.
- Droegemeier, K. K., 1997: The numerical prediction of thunderstorms: Challenges, potential benefits, and

- results from real time operational tests. *WMO Bulletin*, 46, 324-336.
- Gao, J., M. Xue, Z. Wang, and K. K. Droegemeier, 1998: The initial condition and explicit prediction of convection using ARPS forward assimilation and adjoint methods with WSR-88D data. *Preprints, 12th Conf. Num. Wea. Pred.*, Phoenix, AZ, Amer. Meteor. Soc., 176-178.
- Gao, J., M. Xue, A. Shapiro and K. K. Droegemeier, 1999: A Variational Method for the Analysis of Three-Dimensional Wind Fields from Two Doppler Radars. *Mon. Wea. Rev.*, 127, 2128–2142.
- Gao, J., M. Xue, K. Brewster, F. Carr, and K. K. Droegemeier, 2002: New development of a 3DVAR system for a nonhydrostatic NWP model. *Preprint, 15th Conf. Num. Wea. Pred. and 19th Conf. Wea. Anal. Forecasting*, San Antonio, TX, Amer. Meteor. Soc., 339-342.
- Gao, J., M. Xue, K. Brewster, and K. K. Droegemeier, 2004: A three-dimensional variational data assimilation method with recursive filter for single-Doppler radar. *J. Atmos. Oceanic. Technol.*, 21, 457-469.
- Gao, J., K. Brewster, and M. Xue, 2006: A comparison of the radar ray path equation and approximations for use in radar data assimilation. *Adv. Atmos. Sci.*, 23(2), 190-198, 10.1007/s00376-006-0190-3.
- Ge, G. and J. Gao, 2007: Latest development of 3DVAR system for ARPS and its application to a tornadic supercell storm. *22nd Conf. on Weather Analysis and Forecasting/18th Conf. on Numerical Weather Prediction*, Park City, Utah, Amer. Meteor. Soc., 2B.6
- Hu, M., M. Xue, and K. Brewster, 2006a: 3DVAR and cloud analysis with WSR-88D level-II data for the prediction of Fort Worth tornadic thunderstorms. Part I: Cloud analysis and its impact. *Mon. Wea. Rev.*, 134, 675-698.
- Hu, M., M. Xue, J. Gao, and K. Brewster, 2006b: 3DVAR and cloud analysis with WSR-88D level-II data for the prediction of Fort Worth tornadic thunderstorms. Part II: Impact of radial velocity analysis via 3DVAR. *Mon. Wea. Rev.*, 134, 699-721.
- Lilly, D. K., 1990: Numerical prediction of thunderstorms: Has its time come? *Quart. J. Roy. Meteor. Soc.*, 116, 779-798.
- Lin, Y., R. D. Farley and H. D. Orville, 1983: Bulk Parameterization of the Snow Field in a Cloud Model. *Journal of Applied Meteorology*, 22, 1065-1092.
- Klemp, J. B. and R. B. Wilhelmson, 1978: Simulations of right- and left-moving storms produced through storm splitting. *J. Atmos. Sci.*, 35, 1097-1110.
- Klemp, J. B. and R. Rotunno, 1983: A study of the tornadic region within a supercell thunderstorm. *J. Atmos. Sci.*, 40, 359-377
- Klemp, J. B., R. B. Wilhelmson and P.S. Ray, 1981: Observed and numerically simulated structure of a mature supercell thunderstorm. *J. Atmos. Sci.*, 38, 1558-1580.
- Probert-Jones, J.R., 1962: The radar equation in meteorology. *Quart. J. Roy. Meteor. Soc.*, 88, 485-495.

- Purser, R. J., W. Wu, D. F. Parrish, and N. M. Roberts, 2003a: Numerical Aspects of the Application of Recursive Filters to Variational Statistical Analysis. Part I: Spatially Homogeneous and Isotropic Gaussian Covariances. *Mon. Wea. Rev.*, **131**, 1524-1535.
- Purser, R. J., W. Wu, D. F. Parrish, and N. M. Roberts, 2003b: Numerical Aspects of the Application of Recursive Filters to Variational Statistical Analysis. Part II: Spatially Inhomogeneous and Anisotropic General Covariances. *Mon. Wea. Rev.*, **131**, 1536-1548.
- Ray, B., C. Johnson, K. W. Johnson, J. S. Bradberry, J. J. Stephens, K. K. Wagner, R. B. Wilhelmson, and J. B. Klemp, 1981: The morphology of several tornadic storms on 20 May 1977. *J. Atmos. Sci.*, **38**, 1643-1633.
- Rihan, F. A., C.G. Collier, S. P. Ballard and S. J. Swarbrick, 2008: Assimilation of Doppler radial winds into a 3D-Var system: Errors and impact of radial velocities on the variational analysis and model forecasts. *Quart. J. Roy. Meteor. Soc.*, **134**, 1701-1716.
- Salonen K., 2002: Observation operator for Doppler radar radial winds in HiRLAM 3D-Var. *Proc. ERAD*. 405-208.
- Serafin, R. J., and J. W. Wilson, 2000: Operational weather radar in the United States: Progress and opportunity. *Bull. Amer. Meteor. Soc.*, **81**, 501-518.
- Shapiro, A., P. Robinson, J. Wurman, and J. Gao, 2003: Single-Doppler velocity retrieval with rapid scan radar data. *J. Atmos. Oceanic. Technol.*, **20**, 1758-1775.
- Sun, J., D. W. Flicker, and D. K. Lilly, 1991: Recovery of three-dimensional wind and temperature fields from simulated single-Doppler radar data. *J. Atmos. Sci.*, **48**, 876-890.
- Sun, J., and N. A. Crook, 1997: Dynamical and Microphysical Retrieval from Doppler Radar Observations Using a Cloud Model and Its Adjoint. Part I: Model Development and Simulated Data Experiments. *J. Atmos. Sci.*, **54**, 1642-1661.
- Sun, J., and N. A. Crook, 1998: Dynamical and Microphysical Retrieval from Doppler Radar Observations Using a Cloud Model and Its Adjoint. Part II: Retrieval Experiments of an Observed Florida Convective Storm. *J. Atmos. Sci.*, **55**, 835-852.
- Sun, J., and N. A. Crook, 2001: Real-time low-level wind and temperature analysis using single WSR-88D data. *Wea. forecasting*, **16**, 117-132.
- Tong, M., 2006: Ensemble Kalman filter assimilation of Doppler radar data for the initialization and prediction of convective storms. *Ph.D Dissertation at University of Oklahoma*, 263 pages; AAT 3207565
- Weygandt, S. S., A. Shapiro, and K. K. Droegemeier, 2002a: Retrieval of initial forecast fields from single-Doppler observations of a supercell thunderstorm. Part I: Single-Doppler velocity retrieval. *Mon. Wea. Rev.*, **130**, 433-453.
- Weygandt, S. S., A. Shapiro, and K. K. Droegemeier, 2002b: Retrieval of initial forecast fields from single-

Doppler observations of a supercell thunderstorm.  
Part II: Thermodynamic retrieval and numerical prediction. *Mon. Wea. Rev.*, 130, 454-476.

Wood, V. T. and R. A. Brown, 1997: Effects of radar sampling on single-Doppler velocity signatures of mesocyclones and tornadoes. *Weather and forecasting*, 12, 928-938.

Xue, M., K. K. Droegemeier, and V. Wong, 2000: The Advanced Regional Prediction System (ARPS)- A multiscale nonhydrostatic atmospheric simulation and prediction tool. Part I: Model dynamics and verification. *Meteor. Atmos. Physics*, 75, 161-193.

Xue, M., K. K. Droegemeier, V. Wong, A. Shapiro, K. Brewster, F. Carr, D. Weber, Y. Liu, and D. Wang, 2001: The Advanced Regional Prediction System (ARPS) - A multi-scale nonhydrostatic atmospheric simulation and prediction tool. Part II: Model physics and applications. *Meteor. Atmos. Phys.*, 76, 143-166.

Xue, M., D.-H. Wang, J.-D. Gao, K. Brewster, and K. K. Droegemeier, 2003: The Advanced Regional Prediction System (ARPS), storm-scale numerical weather prediction and data assimilation. *Meteor. Atmos. Physics*, 82, 139-170.

Xue, M., M. Tong and K. K. Droegemeier, 2006: An OSSE Framework Based on the Ensemble Square Root Kalman Filter for Evaluating the Impact of Data from Radar Networks on Thunderstorm Analysis and Forecasting. *J. Atmos. Oceanic Technol.*, 23, 46-66.



**Table Caption**

Table 1. List of data analysis/assimilation experiments

## Figure Captions

Fig. 1. The variation of RMS errors with the surface distance between the center of the storm and radar locations, for (a) horizontal wind, and (b) vertical velocity. The solid lines are for CNTL1 experiments, the dashed lines are for the NoBB1 experiments.

Fig. 2. Same as Fig. 1, but the dashed lines are for the NoCV1 experiments.

Fig. 3. Perturbation horizontal winds (vectors,  $\text{ms}^{-1}$ ) and vertical velocity  $w$  (contours,  $\text{ms}^{-1}$ ) at  $t=120$  min and 3.5 km AGL for (a) truth simulation; (b) CNTL1\_60; (c) NoBB1\_60; (d) NoCV1\_60. The  $w$  contour starting from  $5 \text{ ms}^{-1}$  with an interval of  $5 \text{ ms}^{-1}$ .

Fig. 4. Total u-w wind vectors and vertical velocity (contours) of the 20 May 1977 supercell storm at  $t=120$  min and  $y=22.5$  km (along the line A-B in Fig. 3a) for (a) truth simulation; (b) CNTL1\_60km experiment; (c) NoBB1\_60km experiment; (d) NoCV1\_60km experiment.

Fig. 5. Same as Fig. 3, but for (a) CNTL1\_150km experiment; (b) NoBB1\_150km experiment; (c) NoCV1\_150km experiment.

Fig. 6. Same as Fig 4, but for (a) CNTL1\_150km experiment; (b) NoBB1\_150km experiment; (c) NoCV1\_150km experiment.

Fig. 7. The total u-v wind vector, perturbation potential temperature (contour at every 1K) and reflectivity (colored) at  $z=250\text{m}$  AGL and  $t=140\text{min}$ ,  $155\text{min}$ ,  $170\text{min}$  respectively. (a), (b), (c) are for truth simulation, (d), (e), (f) are for CNTLM\_60km experiment, (g), (h), (i) are for NoBBM\_60km experiment, (j), (k), (m) are for NoCVM\_60km experiment. Solid contour for positive, and dashed contour for negative.

Fig. 8. The perturbation u-v wind vector, vertical velocity (contour at every 5m/s) at  $z=3.5\text{km}$  AGL and  $t=140\text{min}$ ,  $155\text{min}$ ,  $170\text{min}$  respectively. (a), (b), (c) are for truth simulation; (d), (e), (f) are for CNTLM\_60km experiment; (g), (h), (i) are for NoBBM\_60km experiment; (j), (k), (m) are for NoCVM\_60km experiment. Solid contour for positive, and dashed contour for negative.

Fig. 9. The evolution of the RMS errors with time for different model variables. The sold lines are for CNTLM\_60km experiment, the dashed lines are for NoBBM\_60km experiment, the dotted lines are for NoCVM\_60km experiment.

Fig. 10. Same as Fig7, but (a), (b), (c) are for CNTLM\_150km experiment, (d), (e), (f) are for NoBBM\_150km experiment, (g), (h), (i) are for NoCVM\_150km experiment. Solid contour for positive, dashed contour for negative.

Fig. 11. Same as Fig 9, but (a), (b), (c) are for CNTLM\_150km experiment, (d), (e), (f) are for NoBBM\_150km experiment, (g), (h), (i) are for NoCVM\_150km experiment. Solid contour for positive, dashed contour for negative.

Fig. 12. The evolution of the RMS error for different model variables. The sold lines are for CNTLM\_150km experiment, the dashed lines are for NoBBM\_150km experiment, the dotted dash lines are for NoCVM\_150km experiment.

Table 1. List of data analysis/assimilation experiments

Name <sup>a</sup>	Radar distance	Description
CNTL_ xxx	20km~220km at an interval of 10km (xxx is the radar distance in km)	one-time analyses at t=2h (21 experiments for each type)
NoBB_ xxx		
NoCV_ xxx		
CNTLM_ 60	60km	One hour assimilation from t=2h~3h at an interval of 5min
NoBBM_ 60		
NoCVM_ 60		
CNTLM_ 150	150km	
NoBBM_ 150		
NoCVM_ 150		

<sup>a</sup>CNTL means both the effects of beam broadening and earth curvature are considered;  
NoBB means the effect of beam broadening are neglected;  
NoCV means the effect of earth curvature are neglected.

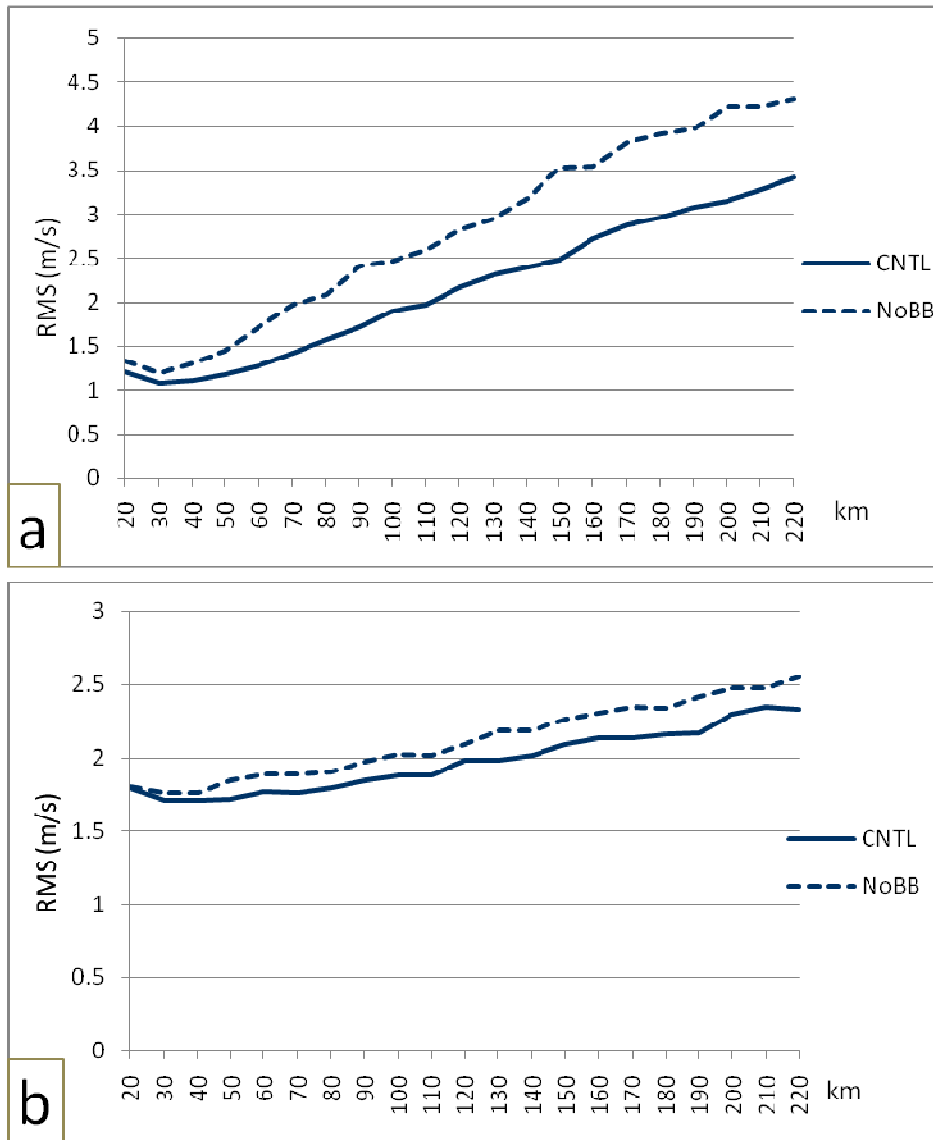


Fig. 1. The variation of RMS errors with the distance between the center of the storm and radar locations, for (a) horizontal wind, and (b) vertical velocity. The solid lines are for CNTL1 experiments, the dashed lines are for the NoBB1 experiments.

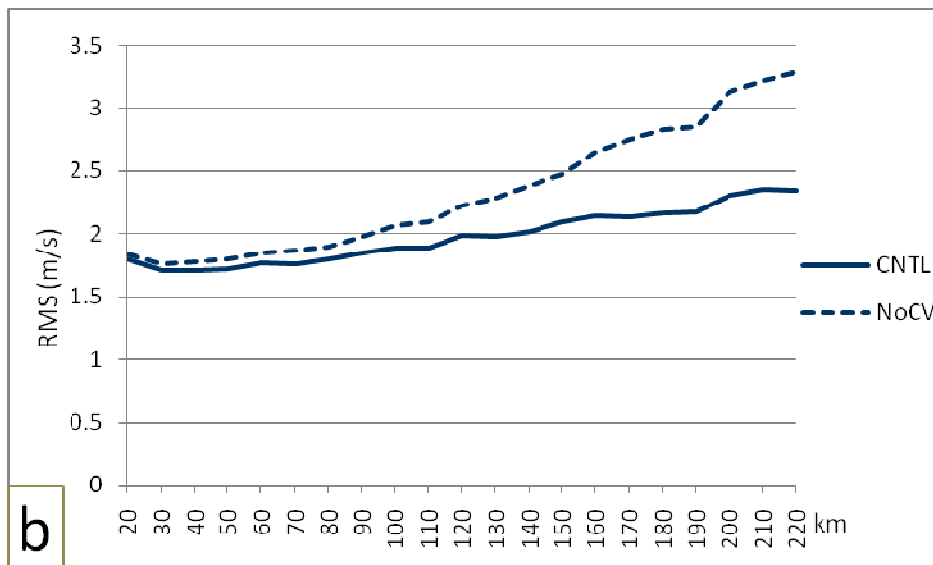
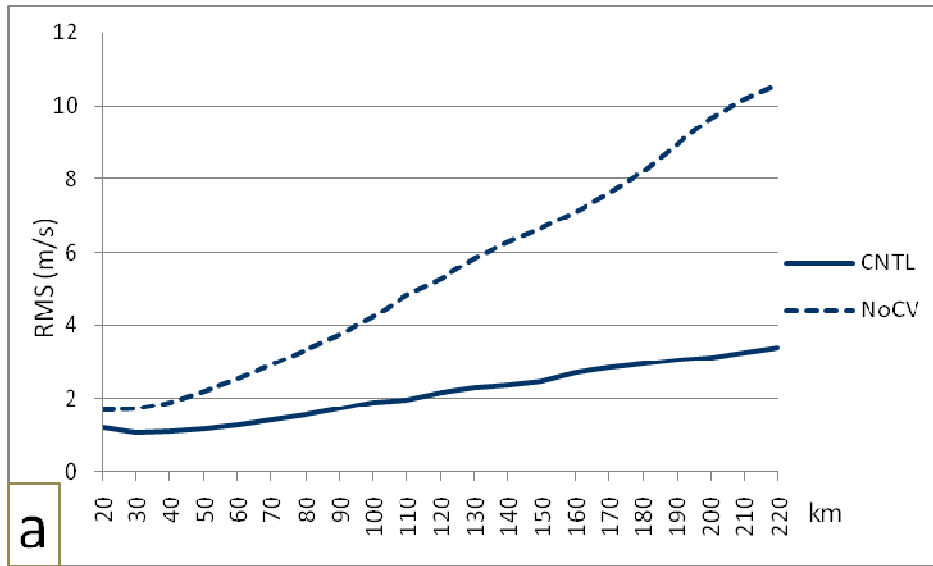


Fig. 2. Same as Fig. 1, but the dashed lines are for the NoCV1 experiments.

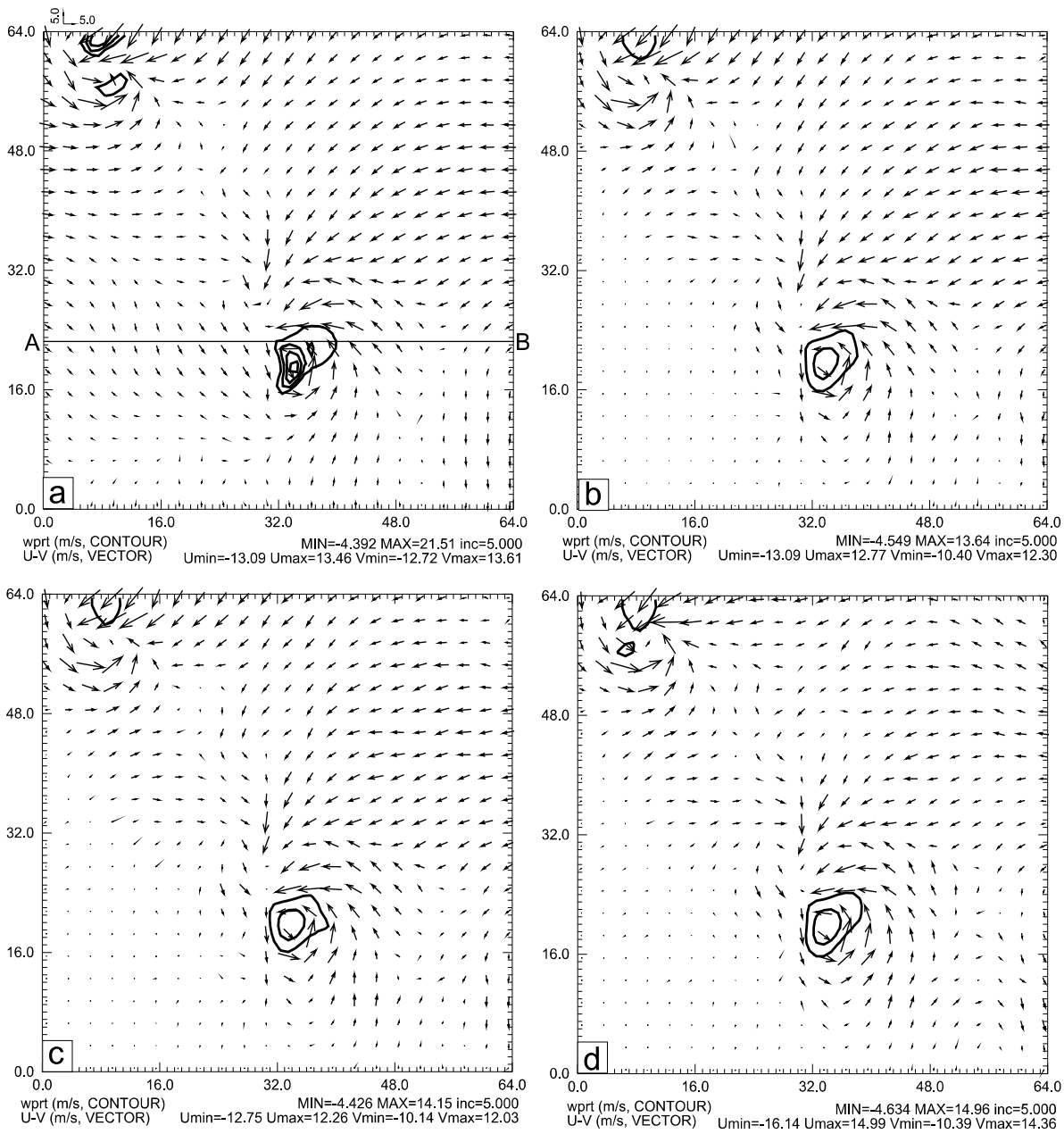


Fig. 3. Perturbation horizontal winds (vectors,  $\text{ms}^{-1}$ ) and vertical velocity  $w$  (contours,  $\text{ms}^{-1}$ ) at  $t=120$  min and 3.5 km AGL for (a) truth simulation; (b) CNTL1\_60; (c) NoBB1\_60; (d) NoCV1\_60. The  $w$  contour starting from  $5 \text{ ms}^{-1}$  with an interval of  $5 \text{ ms}^{-1}$ .

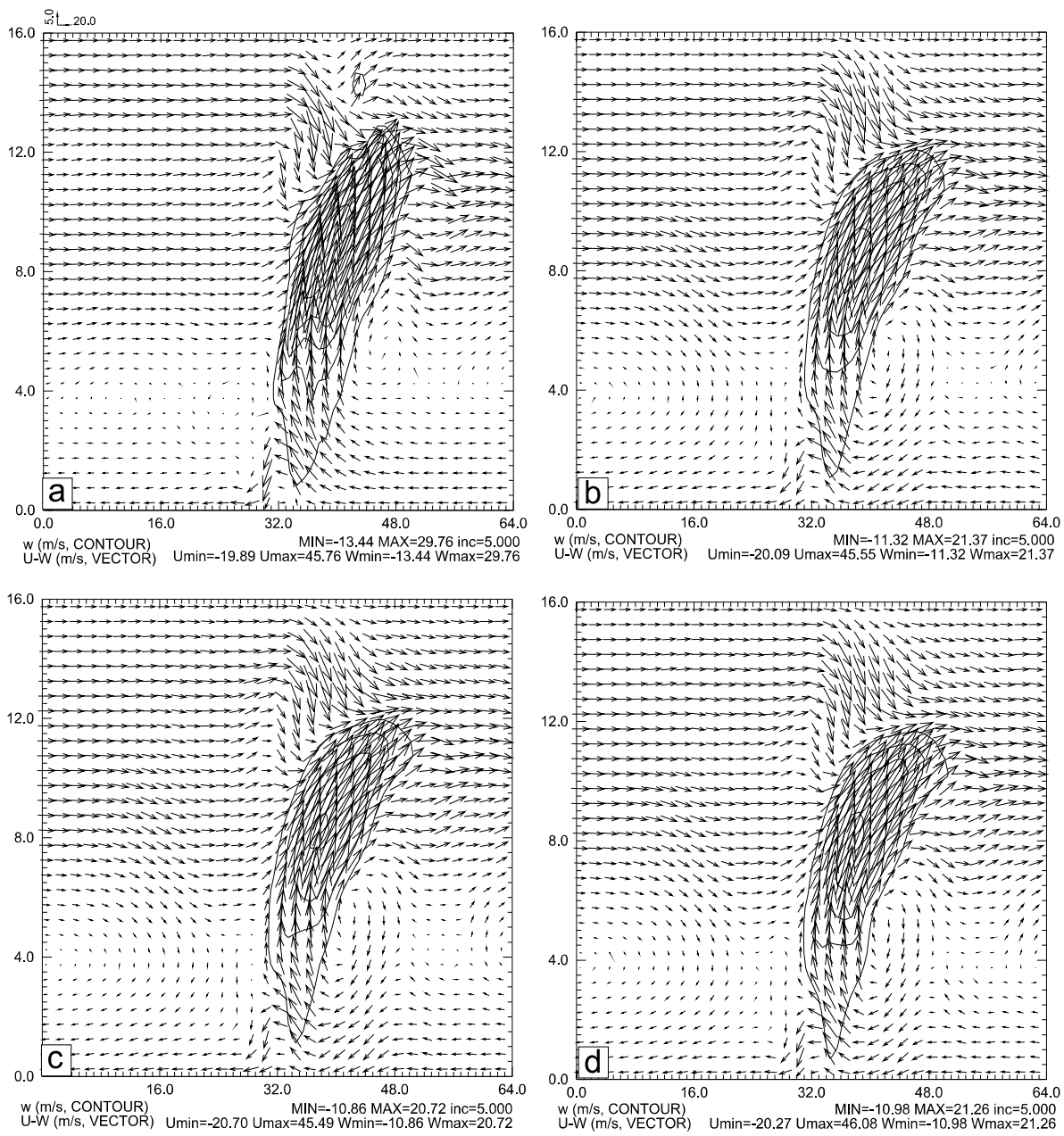


Fig. 4. Total u-w wind vectors and vertical velocity (contours) of the 20 May 1977 supercell storm at t=120 min and y=22.5 km (along the line A-B in Fig. 3a) for (a) truth simulation; (b) CNTL1\_60km experiment; (c) NoBB1\_60km experiment; (d) NoCV1\_60km experiment.

Fig. 5. Same as Fig. 3, but for (a) CNTL1\_150km experiment; (b) NoBB1\_150km experiment; (c) NoCV1\_150km experiment.

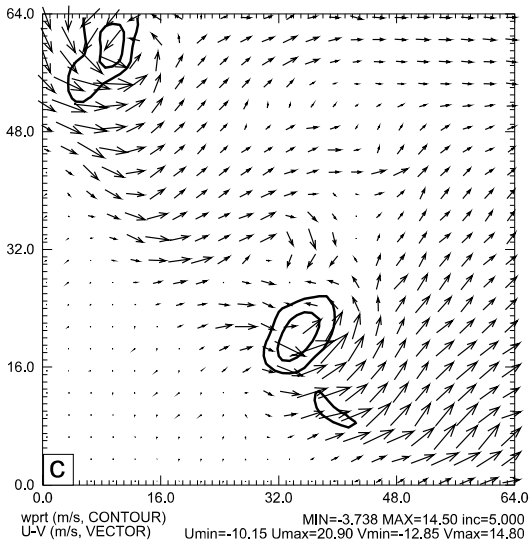
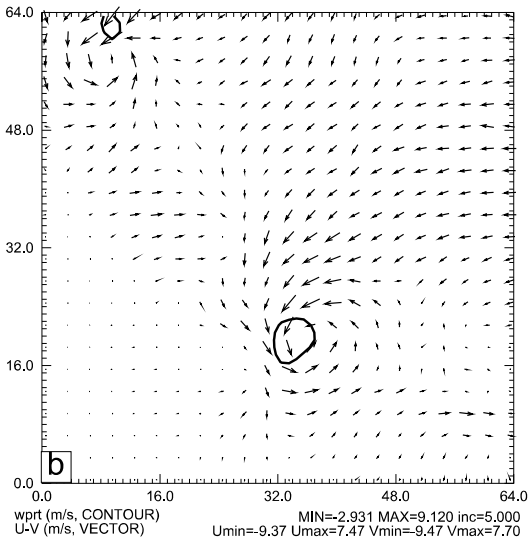
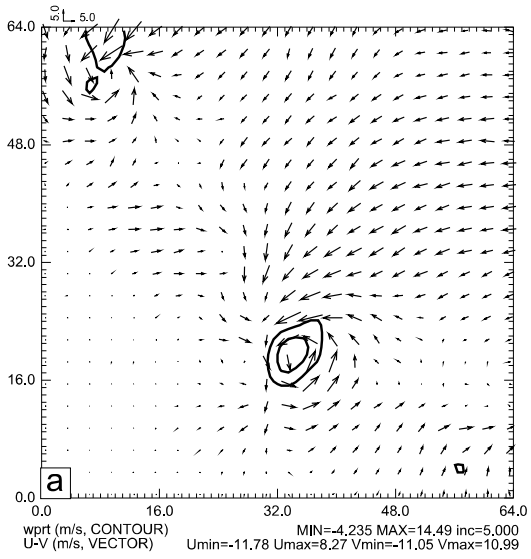
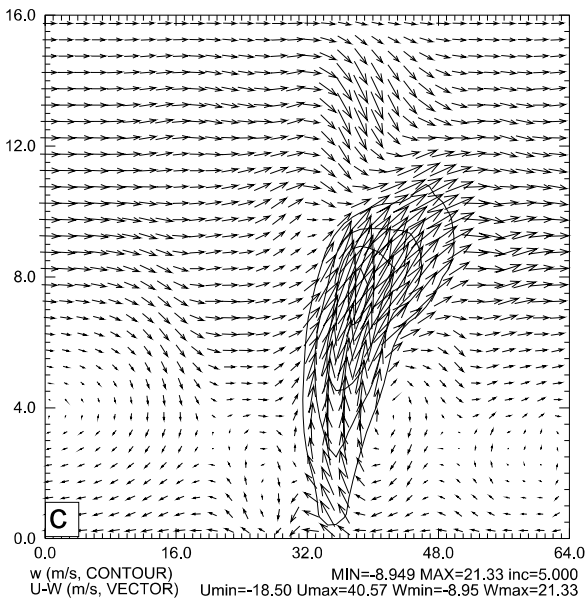
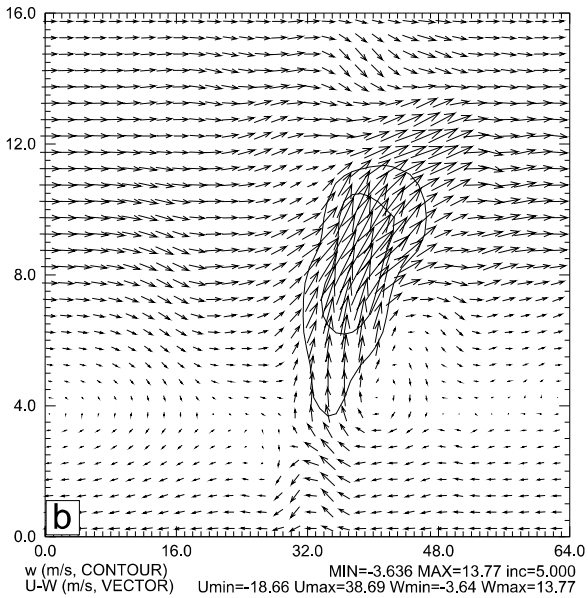
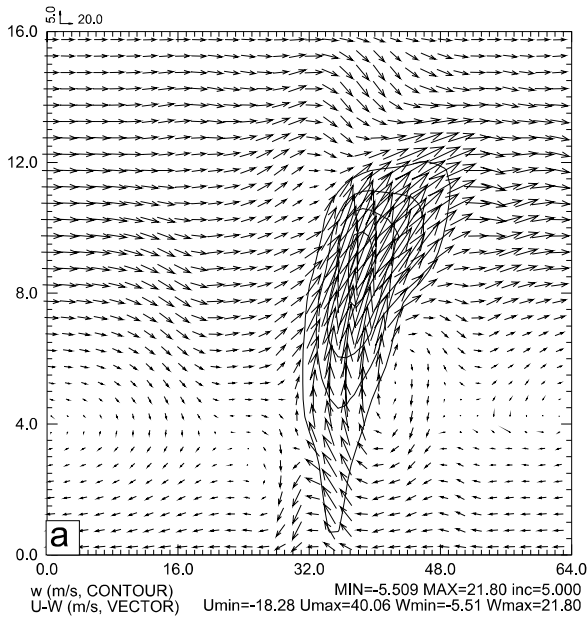


Fig. 6. Same as Fig 4, but for (a) CNTL1\_150km experiment; (b) NoBB1\_150km experiment; (c) NoCV1\_150km experiment.



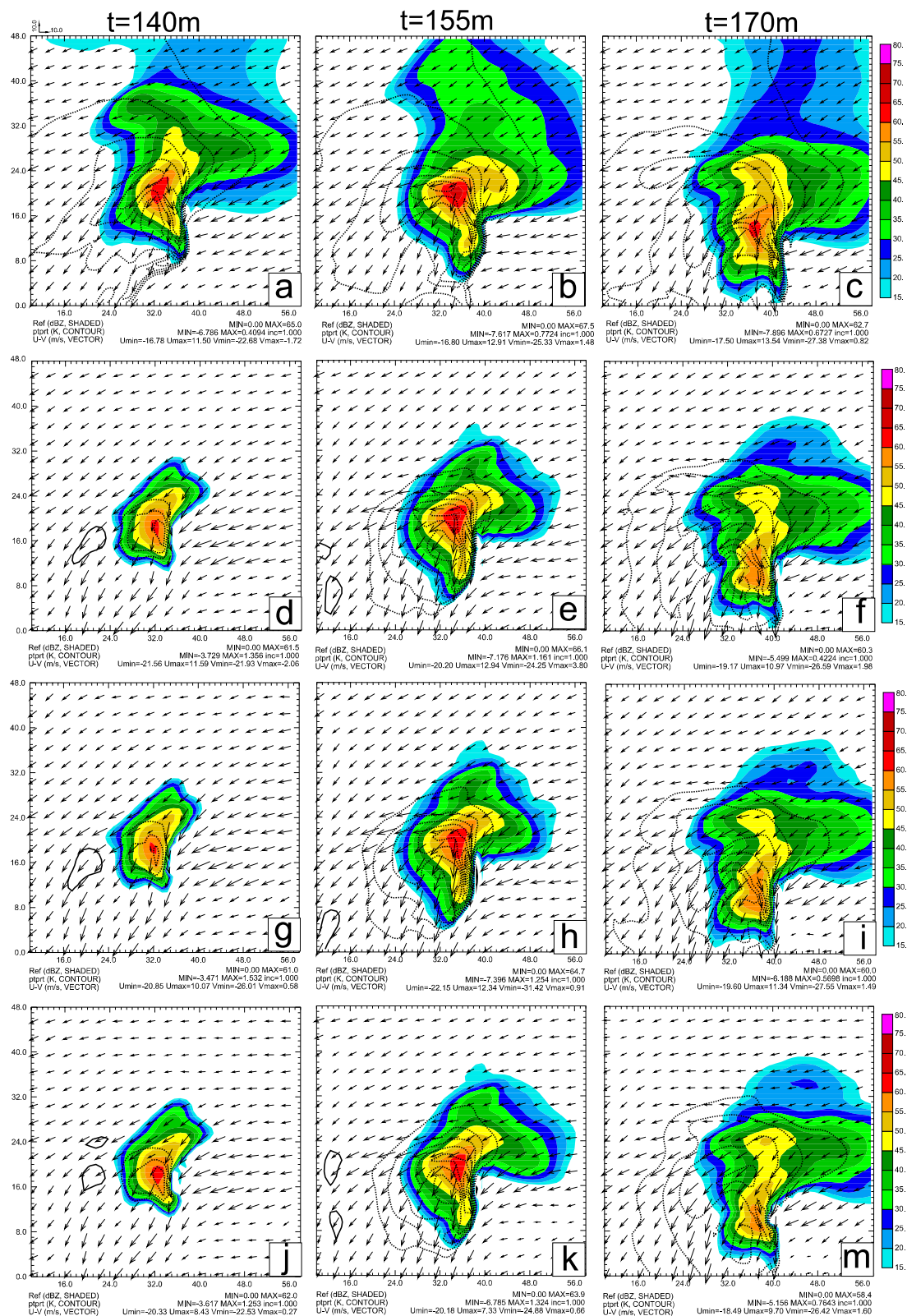


Fig. 7. The total u-v wind vector, perturbation potential temperature (contour at every 1K) and reflectivity (colored) at  $z=250\text{m}$  AGL and  $t=140\text{min}$ ,  $155\text{min}$ ,  $170\text{min}$  respectively. (a), (b), (c) are for truth simulation, (d), (e), (f) are for CNTLM\_60km experiment, (g), (h), (i) are for NoBBM\_60km experiment, (j), (k), (l) are for NoCVM\_60km experiment. Solid contour for positive, and dashed contour for negative.

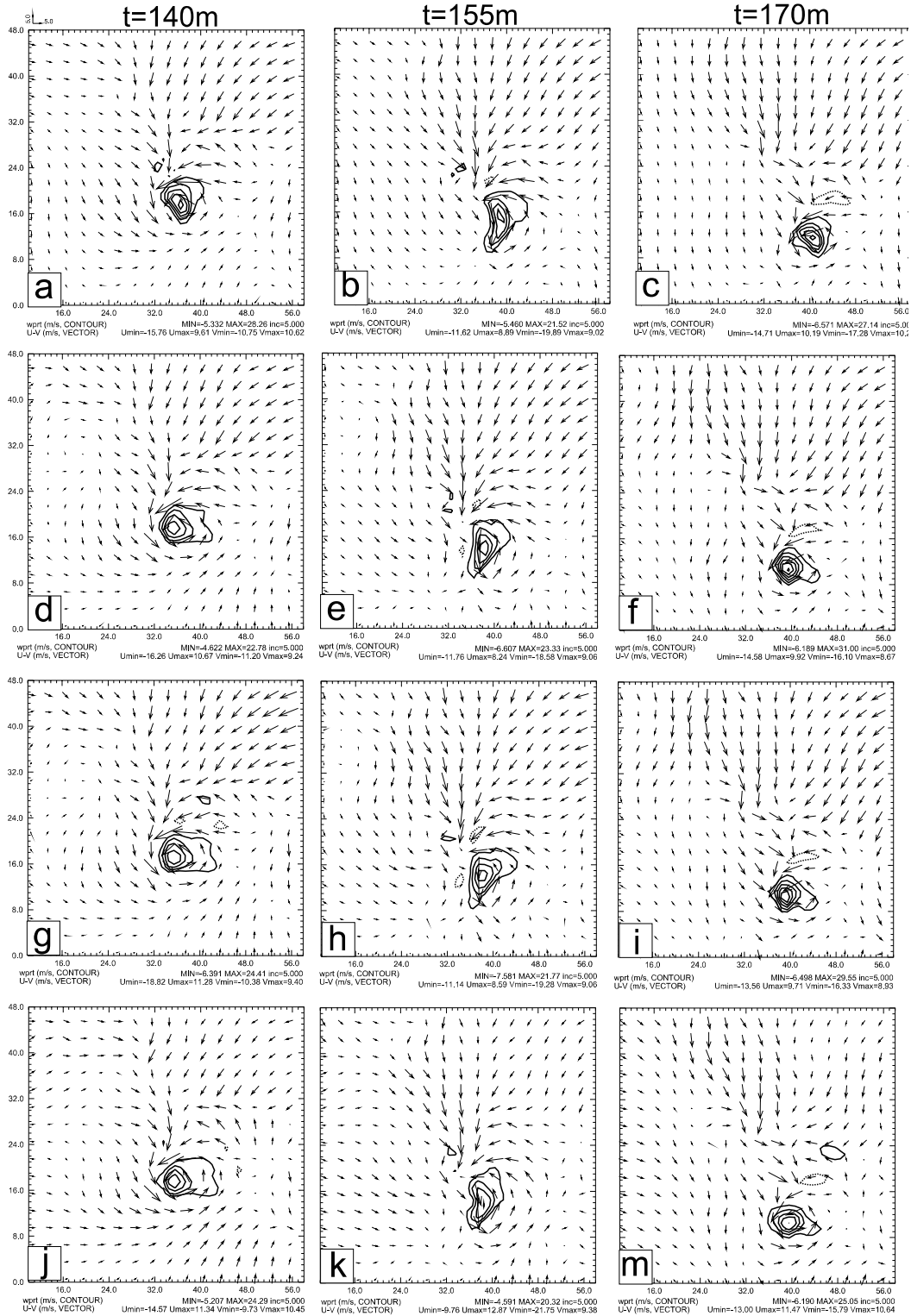


Fig. 8. The perturbation u-v wind vector, vertical velocity (contour at every 5m/s) at  $z=3.5\text{km}$  AGL and  $t=140\text{min}$ ,  $155\text{min}$ ,  $170\text{min}$  respectively. (a), (b), (c) are for truth simulation; (d), (e), (f) are for CNTLM\_60km experiment; (g), (h), (i) are for NoBBM\_60km experiment; (j), (k), (m) are for NoCVM\_60km experiment. Solid contour for positive, and dashed contour for negative.

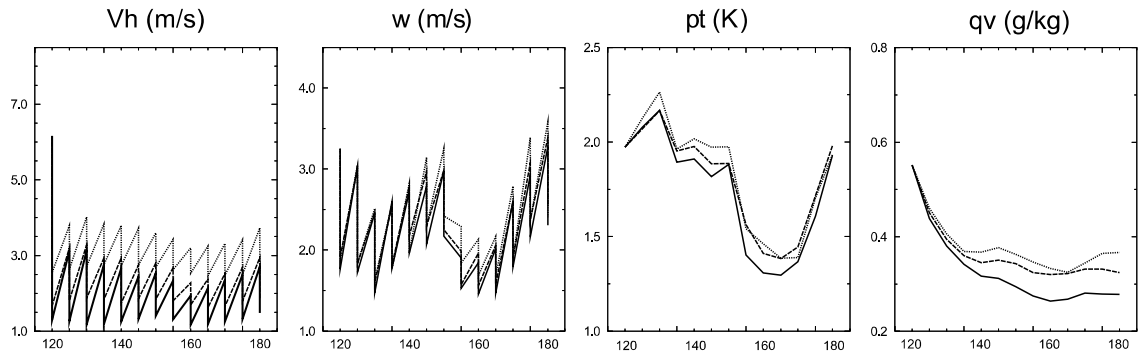


Fig. 9. The evolution of the RMS errors with time for different model variables. The solid lines are for CNTLM\_60km experiment, the dashed lines are for NoBBM\_60km experiment, the dotted lines are for NoCVM\_60km experiment.

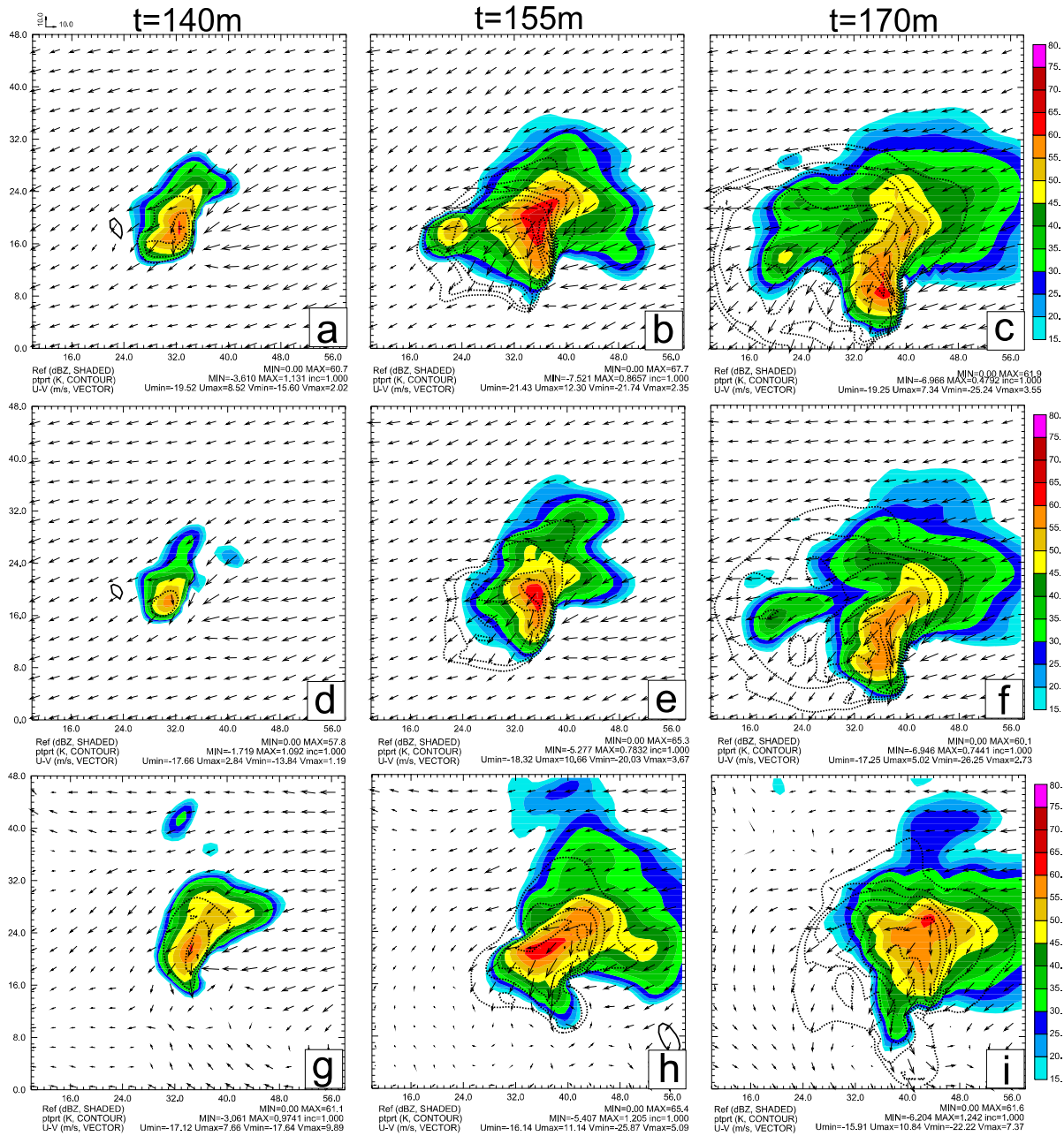


Fig. 10. Same as Fig7, but (a), (b), (c) are for CNTLM\_150km experiment, (d), (e), (f) are for NoBBM\_150km experiment, (g), (h), (i) are for NoCVM\_150km experiment. Solid contour for positive, dashed contour for negative.

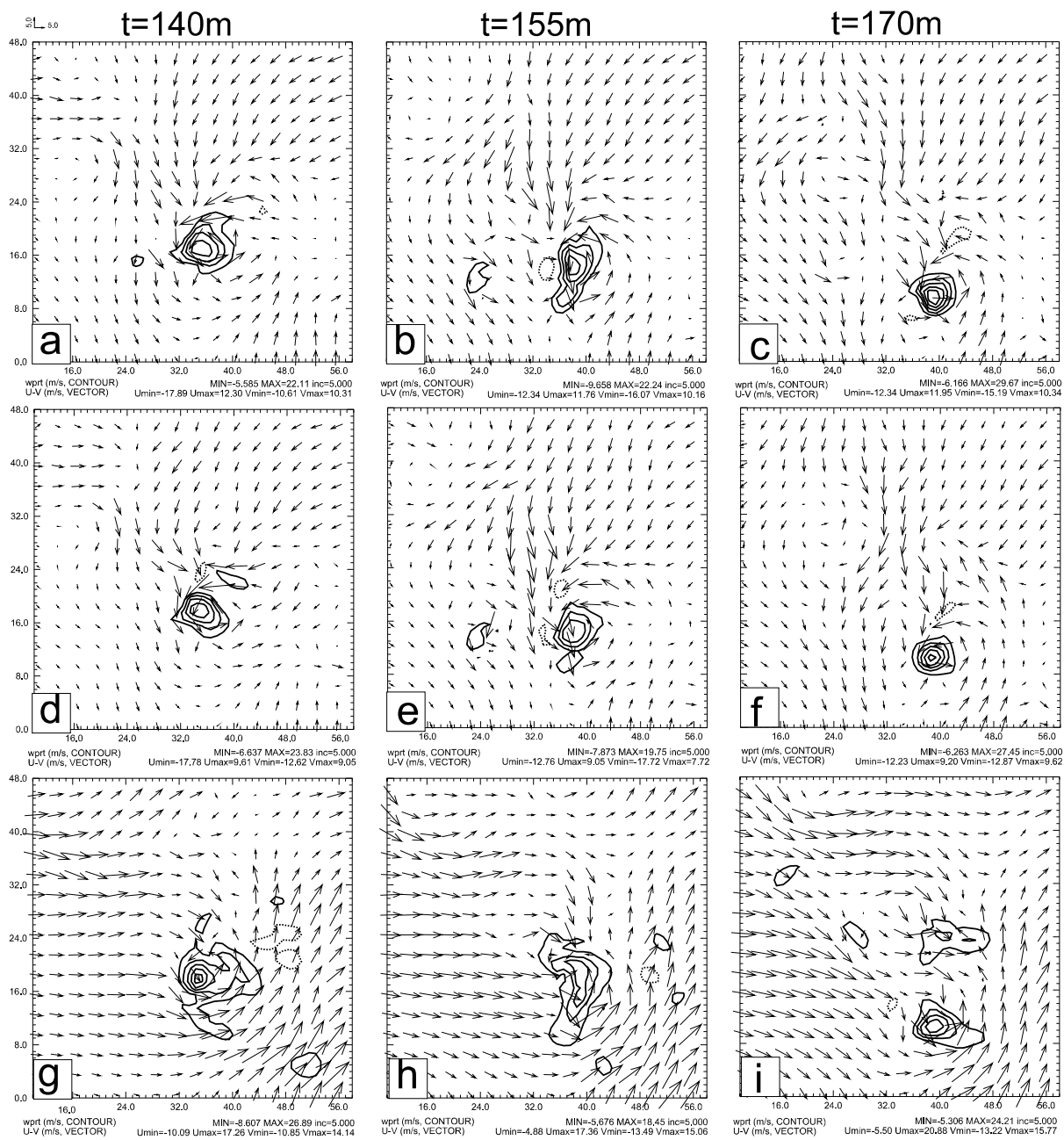


Fig. 11. Same as Fig 9, but (a), (b), (c) are for CNTLM\_150km experiment, (d), (e), (f) are for NoBBM\_150km experiment, (g), (h), (i) are for NoCVM\_150km experiment. Solid contour for positive, dashed contour for negative.

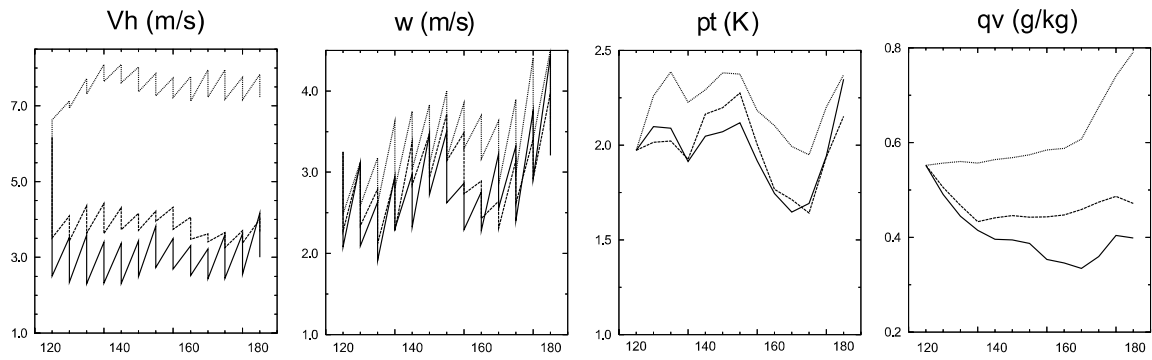


Fig. 12. The evolution of the RMS error for different model variables. The solid lines are for CNTLM\_150km experiment, the dashed lines are for NoBBM\_150km experiment, the dotted dash lines are for NoCVM\_150km experiment.